RESEARCH ARTICLE

small methods
www.small-methods.com

Unveiling the Biologically Dynamic Degradation of Iron Oxide Nanoparticles via a Continuous Flow System

Zhe Yang, Shuwang Wu, Yun Gao, Dandan Kou, Kuan Lu, Can Chen, Yi Zhou, Dandan Zhou, Lei Chen, Jianxian Ge, Cang Li, Jianfeng Zeng, and Mingyuan Gao**

Nanomaterials are increasingly being employed for biomedical applications, necessitating a comprehensive understanding of their degradation behavior and potential toxicity in the biological environment. This study utilizes a continuous flow system to simulate the biologically relevant degradation conditions and investigate the effects of pH, protein, redox species, and chelation ligand on the degradation of iron oxide nanoparticles. The morphology, aggregation state, and relaxivity of iron oxide nanoparticles after degradation are systematically characterized. The results reveal that the iron oxide nanoparticles degrade at a significantly higher rate under the acidic environment. Moreover, incubation with bovine serum albumin enhances the stability and decreases the dissolution rate of iron oxide nanoparticles. In contrast, glutathione accelerates the degradation of iron oxide nanoparticles, while the presence of sodium citrate leads to the fastest degradation. This study reveals that iron oxide nanoparticles undergo degradation through various mechanisms in different biological microenvironments. Furthermore, the dissolution and aggregation of iron oxide nanoparticles during degradation significantly impact their relaxivity, which has implications for their efficacy as magnetic resonance imaging contrast agents in vivo. The results provide valuable insights for assessing biosafety and bridge the gap between fundamental research and clinical applications of iron oxide nanoparticles.

1. Introduction

Nanomaterials have shown great potential in biomedical applications, including diagnosis and therapeutic applications,[1] However, their successful utilization in these fields requires a comprehensive understanding of their in vivo biological effects.[2] When nanomaterials interact with biological components and undergo degradation in the body, safety concerns may arise if they surpass the body's regulatory mechanisms, leading to potential risks such as oxidative stress, cellular immune responses, and carcinogenicity.[3] To address these concerns, the concepts of bioaccessibility and biodurability have been proposed to assess the release of soluble components from nanomaterials and their resistance to physical or chemical erosion, respectively.[4] The solubility and dissolution rate of nanomaterials play crucial roles in determining their bioaccessibility and biodurability.[5] International organizations such as the Organization for Economic Cooperation and Development, the European Chemicals Agency, and the Environmental Protection Agency emphasize the importance of solubility and dissolution rate in determining the fate of nanomaterials and their impacts on organisms.[6] In this scenario, it is imperative to explore the in vivo degradation of nanomaterials and obtain quantitative information on bioaccessibility and biodurability.

The in vivo degradation behavior of nanomaterials with potential biomedical applications has been the subject of extensive research. Several studies have reported observations of nanomaterial degradation at the tissue or cell level, involving various types of nanoparticles such as zinc oxide,[7] iron oxide nanoparticles,[8] and silica nanoparticles.[9] For instance, Gazeau et al. investigated the degradation and the long-term fate of gold/iron nanoheterostructured following intravenous injection in mice. These heterostructures comprised a gold monocrystalline core with a diameter of 4.7 ± 1.0 nm, coated with magnetite or maghemite nanocrystals having an average overall size of 13.4 ± 3.2 nm. The nanocrystals were further modified with poly (maleic anhydride *alt*-1-octadecene). From day 7 to 12 months after injection, they observed gold particles with residual iron oxide resulting from the local dissolution of iron

Z. Yang, S. Wu, Y. Gao, D. Kou, K. Lu, C. Chen, Y. Zhou, D. Zhou, L. Chen, J. Ge, C. Li, J. Zeng, M. Gao
Center for Molecular Imaging and Nuclear Medicine
State Key Laboratory of Radiation Medicine and Protection
School for Radiological and Interdisciplinary Sciences (RAD-X)
Collaborative Innovation Center of Radiological Medicine of Jiangsu Higher Education Institutions
Soochow University
Suzhou 215123, China
E-mail: jfzeng@suda.edu.cn; gaomy@iccas.ac.cn

Z. Yang, K. Lu, Y. Zhou, M. Gao
The Second Affiliated Hospital of Soochow University
Suzhou 215004, China

J. Zeng, M. Gao
Suzhou Xinying Biomedical Technology Co. Ltd.
Suzhou 215000, China

The ORCID identification number(s) for the author(s) of this article can be found under https://doi.org/10.1002/smtd.202301479

DOI: 10.1002/smtd.202301479

oxide in lysosomes. Remarkably, 30 days post-injection the diameters of gold cores decreased to 2–3 nm compared to their initial diameter.[10] Despite these insightful observations, biological experiments fail to provide quantitative information for tracking biotransformation products (e.g., released ions/aggregation products), apart from the cumbersome procedures and sacrifice of a great number of animals, which contradicts the "3R" (Reduce, Refine, and Replace) principle.[11] More importantly, the complexity of the bioenvironment poses great challenges to understanding the critical factors, especially those involved in the in vivo degradation process of nanomaterials. Therefore, abiotic solubility experiments have been developed to reduce the reliance on biological experiments, providing valuable information for in-depth exploration of the in vivo degradation of nanomaterials.

Abiotic dissolution experiments of nanomaterials are categorized into static dissolution experiments and dynamic dissolution experiments. The former is widely used to determine the solubility of nanomaterials by exposing a known mass of solid materials to a fixed volume of simulated physiological medium. Upon dissolving for a period of time, the remaining solid part and the dissolved part are separated for further analysis.[5,8,12] Of note, this static approach may offer inaccurate estimations of solubility because during the actual degradation process, the released ions tend to be continuously removed from the deposited compartments,[13] and once they reach solubility saturation, the dissolution kinetics are greatly altered. Taking advantage of using a more realistic media composition (nonequilibrium), the continuous flow dissolution test can, instead, accurately reflect the true dissolution behavior of nanoparticles exposed in vivo.[14] Continuous flow dissolution testing involves incubating nanomaterials in a stationary chamber for hours to days while subjecting them to a constant flow of simulated medium.[15] During this process, dissolved ions are carried away with the simulated medium, while any remaining undissolved solid particles are isolated within the fixed chamber. Both the fluid phase and solid phase products are then analyzed to obtain quantitative information on bioaccessibility and biodurability. In 2018, Wohlleben et al. proposed a standard operating procedure for a continuous flow dissolution test system (CFS),[16] which has been applied in the dissolution rate assessment of various nanomaterials, such as CuO, $BaSO_4$, and TiO_2.[17] However, it is important to acknowledge that despite the current system's feasibility, there is room for optimization and enhancement, particularly concerning system stability and operational simplicity.

Although abiotic dissolution experiments have been extensively utilized to examine the in vivo degradation behavior of nanomaterials, it is worth noting that existing studies primarily focus on unveiling the impact of specific factors, for instance, to investigate the effect of a specific medium or pathway (e.g., oral pathway)[5,18] and to explore the differences in dissolution rate among nanomaterials with diverse coatings or cores.[19] However, nanomaterials undergo a range of interactions and transformations within the in vivo environment, such as protein adsorption,[20] reduction triggered by substances like ascorbic acid or glutathione (GSH),[21] chelation by compounds like citrate or metal mobilizing proteins,[13] as well as degradation induced by H^+ ions or hydrolytic enzymes during their transition from the extracellular matrix (pH 7–7.5) to mature lysosomes (pH 4.5–4.8).[22] These complex interactions make it challenging to systematically investigate the in vivo degradation of nanomaterials and obtain quantitative information on bioaccessibility and biodurability. Additionally, the lack of uniform methodologies across various studies further complicates result comparability. Currently, there is an insufficient comprehensive discussion on the factors influencing the in vivo degradation behavior of nanomaterials, highlighting the urgent need for quantitative data on bioaccessibility and biodurability. The continuous flow dissolution test system offers a distinct advantage in studying the dissolution kinetics of nanomaterials and conducting a comprehensive evaluation of their biotransformation products in a controlled and efficient manner.

Iron oxide nanoparticles have emerged as a prominent nanomaterial for molecular imaging and targeted therapy due to their superior magnetic properties and biocompatible characteristics.[23] Although considerable research has been conducted to validate their efficacy in the field of biomedicine, it is crucial to shed light on the in vivo degradation behavior and characteristics of degraded products associated with iron oxide nanoparticles. In this study, we propose an optimized continuous flow dissolution test system based on Wohlleben's approach. Based on this system, we systematically investigate the dissolution behavior of iron oxide nanoparticles by utilizing the lysosomal environment of macrophages as a model to quantitatively elucidate the degradation kinetics of iron oxide nanoparticles under various degradation mechanisms, including proton solubilization, protein adsorption, redox reactions, and chelation. Moreover, we also monitored the changes in physiochemical properties of iron oxide nanoparticles following degradation, aiming to obtain quantitative data on their bioaccessibility and biodurability. This study represents a pioneering effort toward establishing a more standardized approach for investigating nanomaterial degradation, setting the stage for precise and comparable results in subsequent research. Additionally, by shedding light on the in vivo degradation behavior and comprehensively characterizing the degraded products, the current work contributes to enhancing the overall biosafety assessment and guiding the responsible and effective use of iron oxide nanoparticles.

2. Results and Discussion

2.1. Continuous Flow Systems (CFS) Design

The CFS used in this study comprises an air compressor, a reservoir, a flow cell, a tempered water bath, a peristaltic pump, and an automatic collector (**Figure 1**). To simplify experimental operations, we replaced the 0.5 m liquid level pressure above the flow cell with an air compressor, as suggested in the CFS proposed by Wohlleben et al.[16] This adjustment helps overcome the resistance caused by the 5 kDa film in the flow cell. Furthermore, we implemented a single pressure source with multiple independent pressure outputs, allowing it to work in conjunction with the flow control system. This setup ensures a consistent flow rate for multiple parallel test groups. Additionally, we designed a new flow cell specifically for incubating nanoparticles (Figure S1, Supporting Information). In this system, dissolved ions were taken away through the membrane on which the remaining solid particles were collected. The detailed parameters of the system can

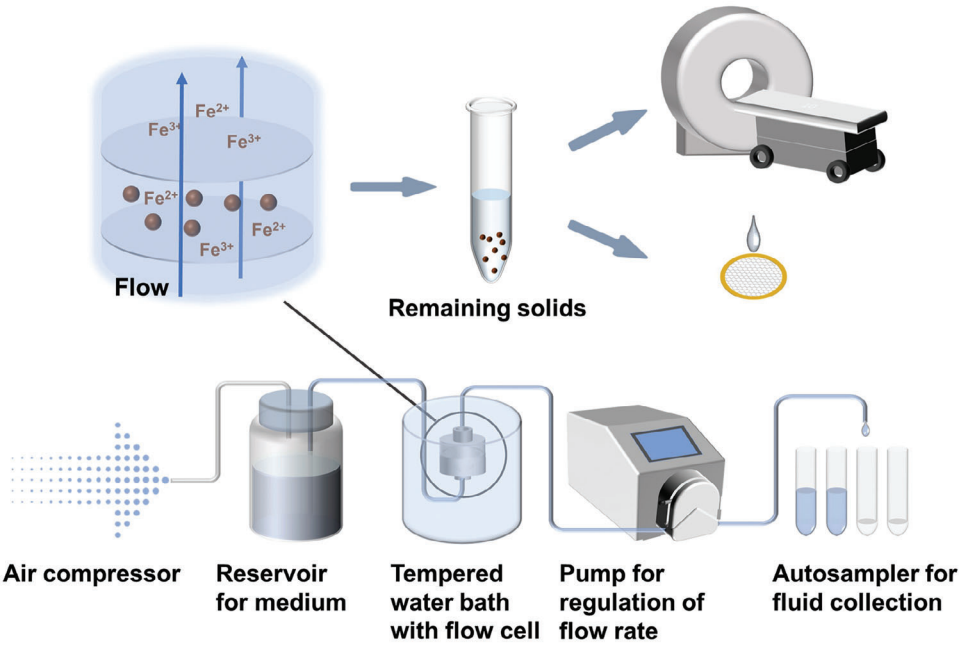

Figure 1. Abiotic continuous flow system (CFS) for nanomaterials. The system consists of an air compressor, a reservoir, a flow cell, a tempered water bath, a peristaltic pump and an automatic collector.

be found in the supporting information. All experiments were performed using 1 mg iron oxide nanoparticles (based on iron content) and a 5 kDa ultrafiltration membrane. The pressure of the air compressor is 45–55 kPa. The flow rate was maintained at 2 mL h^{-1} (Figure S2, Supporting Information). The temperature of the cell was set at 37 °C, and the samples were collected at intervals of 5 h. To evaluate the degradation of iron oxide nanoparticles, the phagolysosomal simulant fluid (PSF)[4] was used and the composition of the PSF is provided in Table S1 (Supporting Information).

2.2. Degradation of Iron Oxide Nanoparticles

2.2.1. Proton-Promoted Dissolution

After being intravenously administered, nanoparticles initially circulate in the bloodstream at a pH level of ≈7.4.[24] Subsequently, they are gradually taken up by various cells. Typically, nanoparticles enter the cell through various endocytic pathways, such as clathrin-mediated endocytosis, caveolae-mediated endocytosis, or macropinocytosis.[25] Once inside the cell, the endosomes that carry the nanoparticles undergo a maturation process. This maturation is accompanied by an increasing acidity within the endosomal compartments, which is facilitated by proton pumps. The pH gradually decreases from a neutral level in early endosomes to ≈6 in late endosomes, and further drops to 4 – 5 in lysosomes.[22] Based on these considerations, we first investigated the degradation of iron oxide nanoparticles in PSF medium at different pH levels of 7.4, 5.5, and 4.5.

PEGylated Fe_3O_4 nanoparticles were synthesized using a thermal decomposition method followed by a ligand exchange process as described in a previous report.[26] The average size of the Fe_3O_4 nanoparticles was determined to be 3.4 ± 0.6 nm through transmission electron microscopy (TEM), as shown in **Figure** 2a. Upon treating the nanoparticles with PSF at different pH values, we observed a gradual erosion of the pristine particles. The average size of the nanoparticles decreased to 3.3 ± 0.8 nm at pH 7.4, 3.2 ± 0.5 nm at pH 5.5, and 2.9 ± 0.5 nm at pH 4.5, indicating the enhanced dissolution of iron oxide nanoparticles in media with lower pH (Figure 2a–d).

The dissolution kinetics and cumulative rate k of iron oxide nanoparticles over a 10-day period showed that the degradation rate of nanoparticles is influenced by the pH of the media, with a higher rate observed at pH 4.5 compared to pH 5.5. However, in a neutral solution, the dissolution of nanoparticles is not obvious (Figure 2e,f). The proton-promoted dissolution mechanism likely explains the increased release of nanoparticles at lower pH levels.[27] For metal oxide materials, the reaction involves a neutralization process between an acid and a weak base (metal oxide), resulting in the production of metal ions and water.[4,28] The initial step of the protonation process is the adsorption of hydrogen protons on the surface of iron oxide nanoparticles, which weakens the iron-oxygen bond and makes the surface hydroxyl group the active site for dissolution.[29] This mechanism selectively removes the active sites on the iron oxide nanoparticle surface, and their number increases as the pH decreases.[31] As depicted in Figure 2g, significant deposition of nanoparticles occurred on the ultrafiltration membrane during dissolution in a neutral medium, whereas no deposition was observed after degradation in acidic media. In the neutral solution, the aggregation of nanoparticles led to a rapid reduction in surface area, resulting in a sharp decrease in active sites, which is another important reason contributing to the limited dissolution. The residual samples collected from solutions with pH 5.5 and 4.5, as shown in Figure 2h, exhibited high stability with a relatively narrow

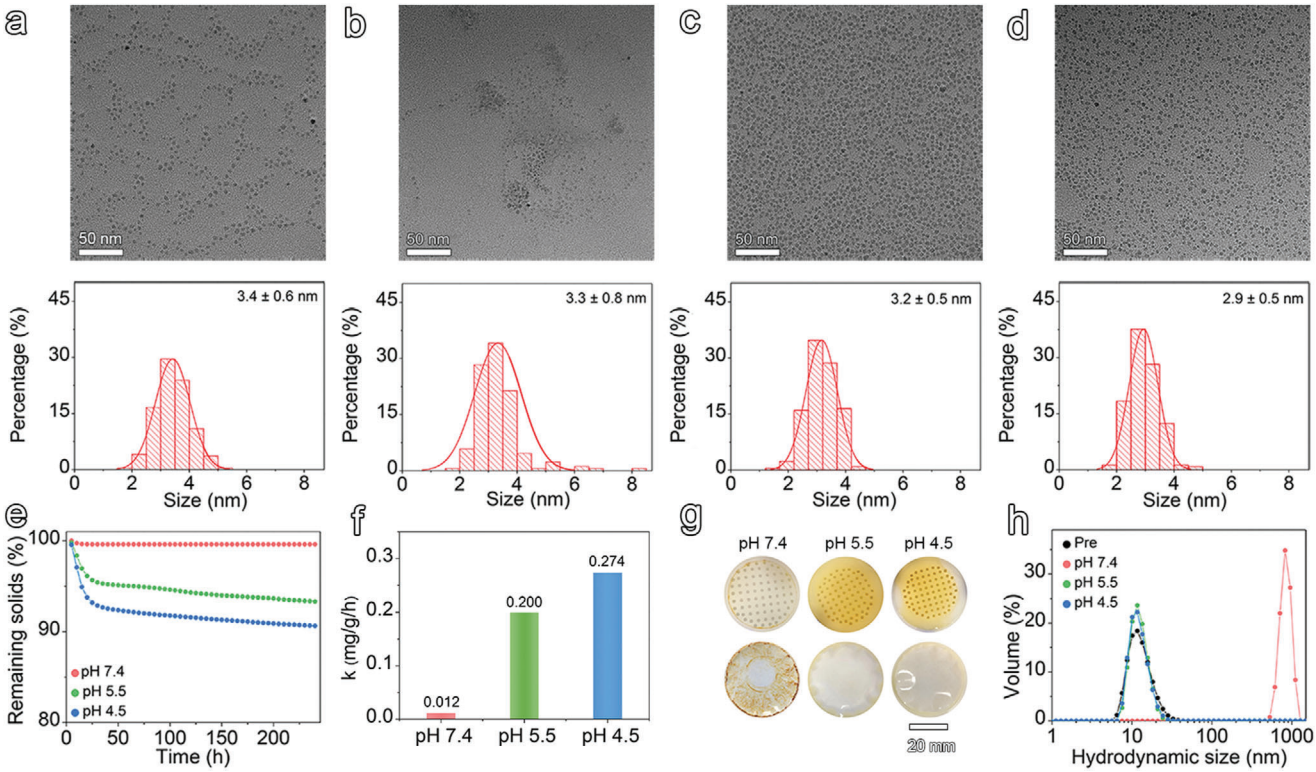

Figure 2. Characterization of Fe_3O_4@DP-PEG nanoparticles after degradation in different pH media for 10 days. The TEM image and size distribution of pristine nanoparticles a) and nanoparticles after degradation in media with pH 7.4 b), 5.5, c) and 4.5 d) for 10 days. The average sizes of iron oxide nanoparticles were obtained by measuring at least 200 nanoparticles. e) Dissolution kinetics of nanoparticles dissolved in media at pH 7.4, pH 5.5, and pH 4.5 for 10 days. f) Cumulative rate *k* of nanoparticles dissolved in different media. g) Optical images of the nanoparticles dissolved in medium with different pH values. It shows the state of solution in the dissolution chamber (upper frame) and the state of deposition of particles on the ultrafiltration membrane (lower frame). h) Hydrodynamic size distribution of pristine nanoparticles and nanoparticles dissolved in different media.

hydrodynamic size distribution peaking at 11.5 and 11.8 nm, respectively, while the nanoparticles experienced aggregation in the neutral solution (826.6 nm). Generally, as the incubation time prolongs, the surface ligands of iron oxide nanoparticles gradually detach and are carried away by the flowing PSF. This detachment of surface ligands reduces the steric hindrance effect, which initially stabilizes the nanoparticles and prevents their aggregation. Consequently, the stability of the nanoparticles will be predominantly governed by electrostatic repulsion. According to the DLVO (Deryaguin, Landau, Verwey, and Overbeek) theory, higher ion concentration or a pH close to the isoelectric point of the particles tends to accelerate particle aggregation.[30] This phenomenon aligns with the study conducted by Baalousha et al., which explored the effect of pH on the aggregation of nanoscale hematite particles and revealed that the aggregation was more significant at pH 6–11, close to the isoelectric point (pH 7.8).[31]

2.2.2. Degration of Nanoparticles Affected by Bovine Serum Albumin (BSA), Glutamine (GSH), and Sodium Citrate (SC)

In addition to pH value, nanoparticles encounter various complex chemical environments after entering the body. Upon interaction with plasma proteins in the circulatory system, nanoparticles form a protein corona.[32] For instance, Grazyna et al. demonstrated that the protein corona of PEGylated iron oxide nanoparticles was enriched in albumin.[33] Furthermore, GSH is known to have higher concentrations in tumor cells compared to normal cells, and numerous nanomaterials have been found to undergo accelerated degradation in the presence of redox (GSH) environments.[34] In addition, SC is naturally present in biological systems at concentrations ranging from 0.1 to 0.3 mM and has been used to simulate the chelation effect of iron-binding proteins during iron mobilization.[4] Therefore, the degradation of iron oxide nanoparticles in PSF media containing BSA, GSH, and SC was investigated. The TEM images of the nanoparticles after degradation for 10 days are shown in **Figure 3**a–c, revealing a decrease in particles size to 3.2 ± 0.6, 2.5 ± 0.4 and 1.4 ± 0.4 nm when incubated with BSA, GSH, and SC, respectively.

The dissolution curves and cumulative rate *k* are shown in Figure 3d,e. The degradation of nanoparticles incubated with BSA exhibited a slower rate compared to degradation in a BSA-free medium with the same pH of 4.5 (0.253 mg h g^{-1} vs 0.274 mg h g^{-1}), indicating that BSA binding contributes to the stability of nanoparticles. This finding is consistent with previous reports by Maccuspie et al.,[35] who observed increased stability when silver nanoparticles were incubated with BSA. The formation of a protein corona on the nanoparticles leads to steric

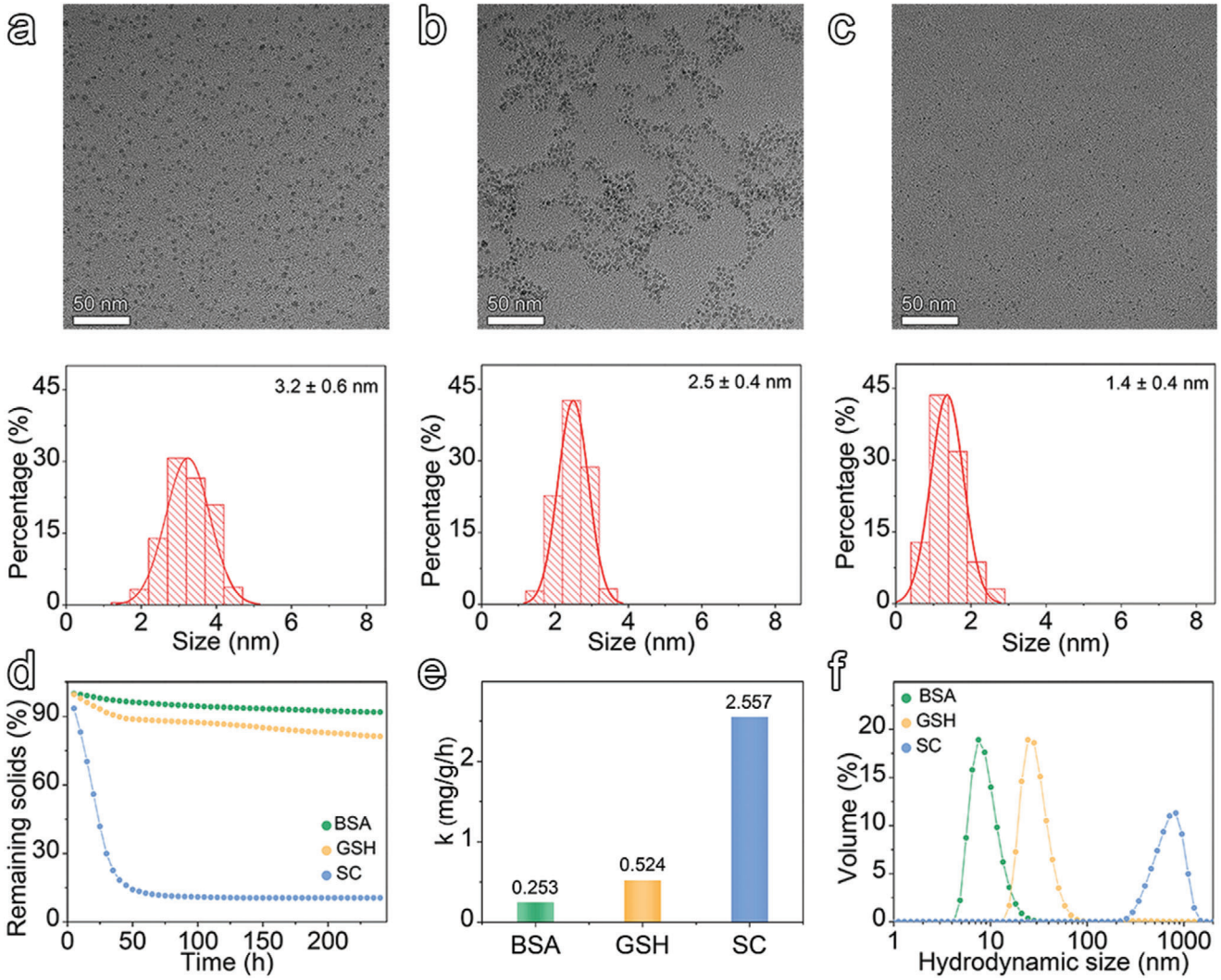

Figure 3. Characterization of Fe_3O_4@DP-PEG nanoparticles after degradation in media containing BSA, GSH, and SC for 10 days. TEM image and size distribution of Fe_3O_4 nanoparticles after 10 days of degradation in medium with BSA a), GSH b), and SC c). All the pH values of the media were adjusted to 4.5. The average sizes of iron oxide nanoparticles were obtained by measuring at least 200 nanoparticles. d) Dissolution kinetics of nanoparticles dissolved in medium with BSA, GSH, and SC for 10 days. The sampling interval was set to 5 h. e) Cumulative rate *k* of nanoparticles dissolved in different media. f) Hydrodynamic size distribution of nanoparticles dissolved in different media.

hindrance,[36] inhibiting the reaction of solutes in solution (dissolved oxygen and/or acidic conditions) with the reactive sites on the surfaces of the nanoparticles.

The percentage of nanoparticle dissolution in the medium containing GSH after 10 days was determined to be 17.3%, with a cumulative dissolution rate of 0.524 mg h g^{-1}, higher than that observed at GSH-free medium with the same pH of 4.5 (0.274 mg h g^{-1}). Both the dissolution curves and cumulative dissolution rate indicate that GSH can accelerate the dissolution of iron oxide nanoparticles, primarily due to its reducing properties. In general, reductive dissolution generally involves an induction period followed by an autocatalytic dissolution period. As a transition metal, iron exists in two oxidation states. Lattice Fe^{II} is more readily transferred to solution than lattice Fe^{III} due to the greater lability (kinetic instability) of the Fe^{II}—O bond. Once Fe^{III} is reduced to Fe^{II} by GSH, it undergoes transformation into Fe^{2+} and gets released. When a sufficient amount of Fe^{2+} accumulates in the solution, autocatalytic dissolution is initiated, thereby accelerating the overall dissolution process.[29b]

In contrast to the effects of BSA and GSH, the presence of SC as a chelating agent in the medium leads to a significant acceleration in the dissolution of iron oxide nanoparticles. After 10 days of incubation, the dissolution percentage reached 89.5%, indicating that only a small portion of the nanoparticles remained undissolved. The cumulative dissolution rate in the presence of SC was 9.10 times higher than that of iron oxide nanoparticles incubated with BSA and 3.88 times higher than that of GSH. The enhanced dissolution might be attributed to the strong chelation between SC and ferric ions, which can remove iron ion complexes adsorbed on the nanoparticle surface, exposing more surfaces for dissolution.[37] Although the three factor has distinct influences on the degradation behavior of iron oxide nanoparticles, it is

noteworthy that there was no deposition of nanoparticles observed after degradation in media containing BSA, GSH, or SC, as depicted in Figure S3 (Supporting Information). The DLS shown in Figure 3g indicated that residual nanoparticles incubated with BSA had a hydrodynamic size of 7.6 nm, probably due to the presence of BSA in the solution. Nanoparticles in the GSH medium exhibit small aggregates, possibly resulting from the ligand shedding of nanoparticles. Furthermore, the DLS analysis of nanoparticles in SC solution showed a hydrodynamic size of 822 nm, indicating that the nanoparticles were almost dissolved, with some remaining aggregates.

Although different factors have varying influences on the degradation behavior of iron oxide nanoparticles, it is interesting to note that the degradation processes consistently exhibit two distinct phases: an initial linear phase followed by a plateau that continues until the end of the experiments. This behavior deviates from the typical first-order kinetics commonly observed in nanomaterials.[38] In our test, the simulated medium continuously washes away the dissolved iron ion, preventing the attainment of dissolution equilibrium. The dissolution effect of iron oxide nanocubes has been reported by Lartigue et al., who observed that the most soluble particles are the first to be degraded, possibly due to defects or the low density of the adsorbed shell. As the shell degrades, the number of defects increases, amplifying the degradation process.[39] We believe that a significant factor contributing to the occurrence of dissolution plateaus in nanomaterials is the change in their internal structure. In magnetic materials, the alteration of the magnetic order on the particle surface and the highly frustrated magnetic coupling in the surface region can lead to the depletion of ferromagnetism. This surface layer is often referred to as the magnetic dead layer.[40] Previous studies by Leyva et al. have demonstrated the presence of a crystalline-ordered core with atomic planes and a surface layer lacking long-range crystalline order in nanoparticles such as $La_{0.67}Sr_{0.33}MnO_3$ and $La_{0.67}Ca_{0.33}MnO_3$.[41] The more structurally stable crystalline-ordered core exhibits higher resistance to dissolution compared to the disordered surface layer, which may contribute to the slowing down of the dissolution rate. Furthermore, as shown in Figure 3c,d, even the most powerful degrading agent, SC, struggles to completely degrade iron oxide nanoparticles. This difficulty may be attributed to the stability of the residual nanoparticles formed during the degradation process. It is reported that the nucleation and growth of nanoparticles involve a wide range of intermediate structures between molecules and solids, including nanoclusters consisting of aggregations of tens to hundreds of atoms. Many of these clusters possess a symmetrically ordered structure that satisfies the all-electron layer structure, and nanoclusters with a specific number of aggregated atoms exhibit special stability.[42] As iron oxide nanoparticles undergo degradation, they have the potential to form highly stable nanoclusters with similar structures. This could explain why nanoparticles in the SC medium cannot be completely degraded.

2.2.3. Relaxivity Evolution of Iron Oxide Nanoparticles under Degradation

Iron oxide nanoparticles are commonly used as magnetic resonance contrast agents in various applications.[26,43] To assess the effect of degradation on the imaging effectiveness of these nanoparticles, we conducted relaxivity measurements on the degraded samples. As illustrated in **Figure 4**a,b, the original iron oxide nanoparticles exhibited a longitudinal relaxivity (r_1) of 2.9 mM^{-1} s^{-1} and a transverse relaxivity (r_2) of 13.8 mM^{-1} s^{-1}. Interestingly, the r_1 values of the nanoparticles incubated in acidic media with pH 5.5 and 4.5 were found to be the same, measuring 3.0 mM^{-1} s^{-1}, while the r_2 values were 14.8 and 16.9 mM^{-1} s^{-1}, respectively. However, measuring the relaxivity of nanoparticles incubated at pH 7.4 was not feasible due to a significant amount of nanoparticle deposition. Nevertheless, the results suggest that the relaxivities of the iron oxide nanoparticles undergo only slightly change following degradation in acidic media. Furthermore, the *T*1- and *T*2-weighted MR images shown in Figure 4c,d suggested that dissolution in acidic media had an insignificant impact on the signals in the region of interest.

In contrast with the negligible effect of acidic erosion, the incubation of nanoparticles with BSA resulted in a significant decrease in r_1, measuring 2.5 mM^{-1} s^{-1}, and a slightly increase in r_2, measuring 14.9 mM^{-1} s^{-1}. Conversely, when the nanoparticles were dissolved with GSH, r_1 decreased to 2.6 mM^{-1} s^{-1}, while r_2 exhibited a dramatic increase to 48.2 mM^{-1} s^{-1}. Generally, the relaxation rate of iron oxide contrast agents is influenced by various factors such as the degree of surface metal ion exposure of nanoparticles, water diffusion coefficient, particle radius, saturation magnetization, and aggregation state.[26,44] In the case of nanoparticles incubated with BSA, the limited dissolution within the BSA-containing media results in minimal changes in particle radius and saturation magnetization. The observed decrease in r_1 can be attributed to the formation of a "protein corona", which reduces the exposure of metal ions on the particle surfaces. Additionally, the slight increase in r_2 can be explained by the adsorption of proteins, which slows the diffusion of water protons around nanoparticles.[45] On the other hand, the decrease in r_1 and increase in r_2 of nanoparticles in the GSH solution can be attributed to the aggregation of particles,[46] as supported by the DLS results shown in Figure 3f. The aggregation of nanoparticles induces changes in the local magnetic field, leading to altered relaxation properties and subsequently affecting the measured relaxivities and *T*1- and *T*2-weighted images (Figure 4c,d).

With respect to the impact of SC chelation on the relaxivity of iron oxide nanoparticles, it was challenging to obtain valuable information due to the aggregation of the residual samples (Figure 3f). Therefore, we conducted further investigations to explore the effects of SC on the particle size and aggregation state of the nanoparticles during incubation. The residual nanoparticles were collected and subjected to characterization after being incubated in SC medium for various durations. The TEM images, as shown in Figure S5 (Supporting Information), revealed that the nanoparticles dissolved quickly within the first 20 h. The diameter of the nanoparticles decreased from an initial size of 3.4 ± 0.6 to 2.8 ± 0.5 nm at 10 h and further to 2.2 ± 0.5 nm at 20 h. In addition, the hydrodynamic size exhibited a reduction from 11.8 to 10.1 nm at 10 h, and to 7.5 nm at 20 h. Remarkably, despite undergoing degradation, the nanoparticles remained stable in the solution and exhibited a relatively narrow distribution of hydrodynamic sizes, providing a solid foundation for investigating the effect of SC chelation on the relaxivity of the iron oxide nanoparticles. The results from the magnetic resonance imaging (MRI)

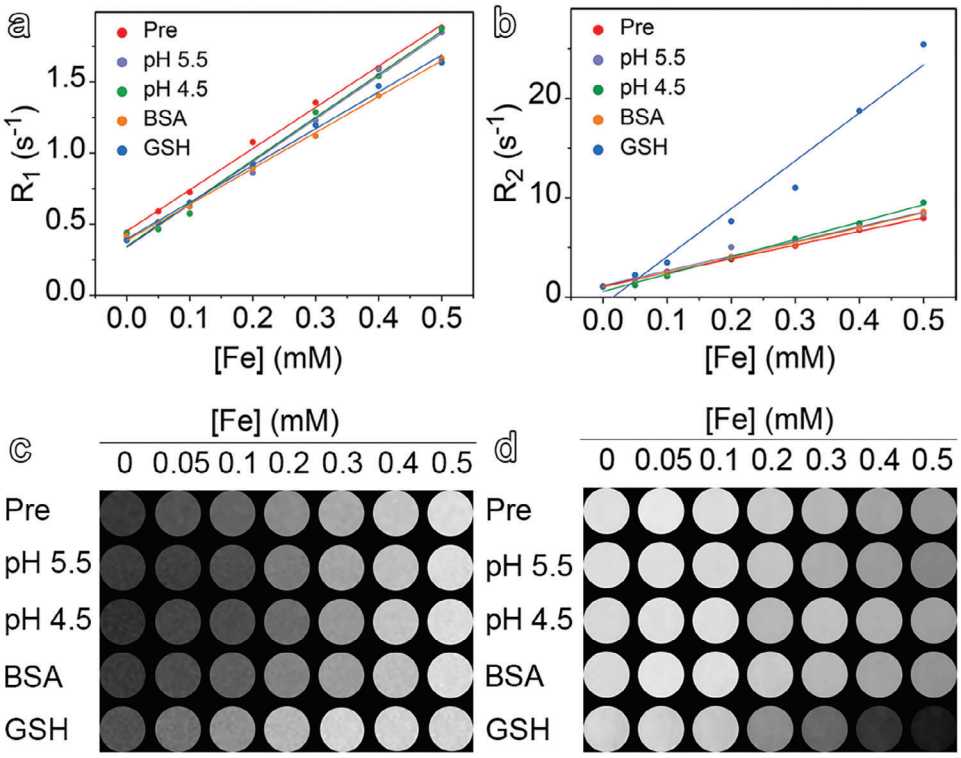

Figure 4. Relaxivity and T_1- and T_2-weighted MR images. Relaxivity of pristine nanoparticles and nanoparticles after degradation in medium with pH 5.5 and 4.5 or medium containing BSA and GSH. The longitudinal relaxivity a) and transverse relaxivity b) extracted from the linear regression fitting of the experimental data. T_1 _ weighted MR images c) and T_2–weighted MR images d) of the pristine nanoparticles and nanoparticles after degradation in the medium with pH 7.4, 5.5, and 4.5 or the medium containing BSA and GSH.

measurements of nanoparticles dissolved in SC at 10 and 20 h are shown Figure S6 (Supporting Information). It is observed that the r_1 initially increases to 4.3 mM^{-1} s^{-1} and then decreases to 2.9 mM^{-1} s^{-1}, which is equivalent to the r_1 value of the nanoparticles before dissolution. On the other hand, the r_2 gradually decreases during the degradation process, with values decreasing from 13.8 to 9.0 mM^{-1} s^{-1} and further to 5.6 mM^{-1} s^{-1}. The increase in r_1 of nanoparticles in the SC medium at 10 h can be attributed to the increased exposure of metal ions with the particle size decrease. However, as the degradation progresses, the iron oxide core of the nanoparticles degrades, leading to a decrease in their saturated magnetization and, consequently, a decrease in r_1 at 20 h. Meanwhile, r_2 continues to decrease throughout the degradation process.

2.2.4. Degradation of the Size Effect

Iron oxide nanoparticles of different sizes have different applications. To investigate the effect of particle size on the degradation behavior of iron oxide nanoparticles, PEGylated iron oxide nanoparticles with a size of 12.1 nm were synthesized (Figure S7, Supporting Information). After being incubated in different media, the TEM images showed a gradual erosion of the pristine particles. The average size of the nanoparticles decreased to 11.9 ± 0.8 nm at pH 7.4, 11.6 ± 0.8 nm at pH 5.5, and 11.6 ± 1.1 nm at pH 4.5 (Figure S7b–d, Supporting Information). Furthermore, when exposed to BSA, GSH, and SC, the particle sizes decreased to 11.7 ± 0.7, 10.3 ± 0.9, and 1.9 ± 0.4 nm, respectively (Figure S8a–c, Supporting Information). Interestingly, although the larger nanoparticles also undergo degradation, their dissolution rate is slower compared to 3.4 nm-sized nanoparticles, as depicted in **Figure 5**. The reduced dissolution rates can be attributed to a decrease in reactive surface site and a decrease in surface Gibbs free energy.[47] In other words, larger particles dissolve more slowly than smaller particles, or the former do not dissolve while the latter does.[48] Furthermore, the propensity of larger counterparts to aggregate within the degradation process can also contribute to the reduced dissolution rate. As shown in Figures S9 and S10 (Supporting Information), the larger nanoparticles exhibited a more pronounced tendency to deposit in media with pH 7.4 and 5.5, as well as in acidic media containing BSA and GSH. This accelerated deposition might be attributed to the influence of gravity, which promotes the settling of larger particles. Due to the deposition of nanoparticles, it is infeasible to determine the relaxometric properties of the degraded samples. However, in the case of nanoparticles incubated in acidic media with pH 4.5, where no significant deposition was observed but slight aggregation was revealed by DLS analysis (Figure S11, Supporting Information), the r_1 value was decreased from 3.5 to 2.1 mM^{-1} s^{-1} while the r_2 value increased from 44.6 to 63.3 mM^{-1} s^{-1} (Figure S12, Supporting Information). The results are consistence with the previous publications, which have reported that the aggregation of iron oxide

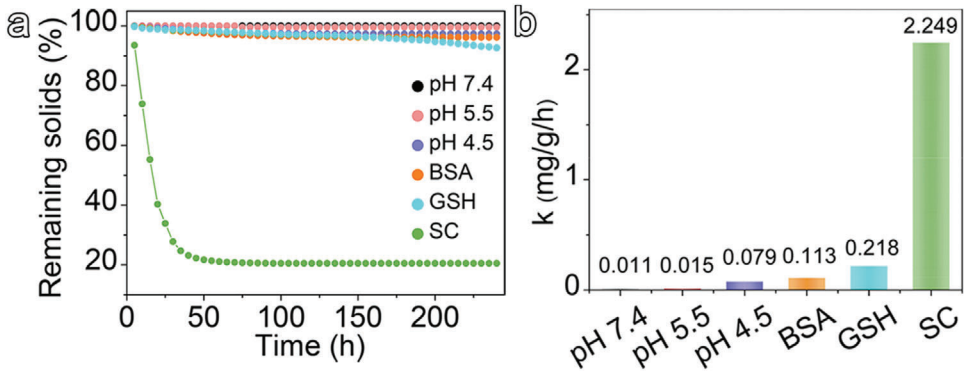

Figure 5. Degradation kinetics a) and dissolution rate *k* b) of 12.1 ± 0.8 nm iron oxide nanoparticles dissolved in different media for 10 days.

nanoparticles tends to lead to a decrease in r_1 and an increase in r_2[49]

It is worth noting that in previous studies, researchers often used the intensity of MRI signals to evaluate the accumulation of iron oxide nanoparticles at the site of lesions.[8,50] However, our findings indicate that upon entering the body, iron oxide nanoparticles experience alterations in their relaxometric properties due to degradation and aggregation in the complex physiological environment. These changes have the potential to impact the accuracy of result assessments. Therefore, accurate evaluation of results based on MRI signal intensity analysis requires careful consideration, particularly when dealing with larger-sized iron oxide nanoparticles, as they are more prone to aggregation, ultimately affecting their relaxometric properties.

3. Conclusion

In summary, we explored the impacts of pH, BSA, GSH, and SC on the degradation of different-sized iron oxide nanoparticles, considering factors such as dissolution kinetics, morphological changes, aggregation states, and relaxivity. The results showed that the degradation of nanoparticles was found to be pH-dependent, with lower pH resulting in faster degradation. Notably, iron oxide nanoparticles incubated with BSA exhibited excellent stability and lower dissolution rates. In contrast, GSH demonstrated the ability to rapidly degrade the nanoparticles, while SC showed the fastest degradation rate. The aggregation of iron oxide nanoparticles in neutral solutions and GSH solution significantly affected the relaxivity of contrast agents, and the surface proteins adsorption led to an obvious decrease in r_1. These findings emphasize the importance of considering aggregation effects and protein adsorption when assessing the relaxivity of iron oxide nanoparticles in different environments. Additionally, it is found that the internal structure alteration during degradation impacted the dissolution behavior of nanomaterials. The proposed experimental conditions offer a predictive model for understanding in vivo degradation and are valuable for future studies. Overall, this study contributes to a comprehensive understanding of the degradation behavior of iron oxide nanoparticles under different conditions and provides important insights for the design and evaluation of nanomaterial-based applications. Nonetheless, it is crucial to acknowledge that the true complexity of the biological milieu far exceeds the experimental representation. More intricate factors, such as the potential influence of enzymes on nanoparticle degradation kinetics, are valuable aspects that warrant comprehensive investigation in future studies.

Supporting Information

Supporting Information is available from the Wiley Online Library or from the author.

Acknowledgements

Z.Y. and S.W. contributed equally to this work. This research was funded by the National Key Research and Development Program of China (2018YFA0208800), the National Natural Science Foundation of China (82130059, 82222033, and 82172003), the Suzhou Key Industry Technology Innovation Projects (SYG202036), Leading Talents of Innovaion and Entrepreneurship of GuSu (ZXL2022482), the Natural Science Foundation of Jiangsu Province (BK20220508), and Priority Academic Program Development of Jiangsu Higher Education Institutions (PAPD).

Conflict of Interest

The authors declare no conflict of interest.

Data Availability Statement

The data that support the findings of this study are available from the corresponding author upon reasonable request.

Keywords

continuous flow system, degradation, iron oxide nanoparticles, nanomaterials

Received: October 25, 2023
Revised: November 11, 2023
Published online: November 27, 2023

[1] a) N. Baig, I. Kammakakam, W. Falath, *Mater. Adv.* **2021**, *2*, 1821; b) Y. H. Zhang, K. Poon, G. S. P. Masonsong, Y. Ramaswamy, G. Singh,

Pharmaceutics **2023**, *15*, 20; c) L. Yan, B. Qing, Y. Shuxu, Y. Mingying, M. Chuanbin, *View*. **2022**, *3*, 20200027; d) Y. Jing, H. Lin, K. Qian, *Exploration* **2022**, *2*, 20210222; e) Y. Jing, Y. Xia, Z. Longzhou, Z. Xiwen, L. Yue, Z. Linzhou, L. Wanshan, Z. Ru, Y. Xuecheng, S. Li, D. Wen, F. Lei, J. Yi, W. Jinlan, Q. Kun, Y. Xiaodong, *Adv. Mater.* **2022**, *34*, 2201422.

[2] C. Dragar, S. Kralj, P. Kocbek, *Int. J. Pharm*. **2021**, *597*, 120348.

[3] R. Mohammapdour, H. Ghandehari, *Adv. Drug Delivery Rev.* **2022**, *180*, 114022.

[4] E. Innes, H. H. P. Yiu, P. Mclean, W. Brown, M. Boyles, *Crit. Rev. Toxicol*. **2021**, *51*, 217.

[5] P. Bove, M. A. Malvindi, S. S. Kote, R. Bertorelli, M. Summa, S. Sabella, *Nanoscale* **2017**, *9*, 6315.

[6] a) European Chemicals Agency, https://doi.org/10.2823/273911 (accessed: October 2019); b) Organisation for Economic Co-operation and Development, https://one.oecd.org/document/ENV/JM/MONO(2010)46/en/pdf; c) N. I. B. Hartmann, L. M. Skjolding, S. F. Hansen, A. Baun, J. Kjølholt, F. Gottschalk, *Environ. Prot. Agency* **2014**, *1594*.

[7] V. A. Senapati, A. Kumar, *Environ. Chem. Lett.* **2018**, *16*, 1129.

[8] I. V. Zelepukin, A. V. Yaremenko, I. N. Ivanov, M. V. Yuryev, V. R. Cherkasov, S. M. Deyev, P. I. Nikitin, M. P. Nikitin, *ACS Nano*. **2021**, *15*, 11341.

[9] S. P. Hadipour Moghaddam, R. Mohammadpour, H. Ghandehari, *J. Controlled Release*. **2019**, *311*, 1.

[10] J. Kolosnjaj-Tabi, Y. Javed, L. Lartigue, J. Volatron, D. Elgrabli, I. Marangon, G. Pugliese, B. Caron, A. Figuerola, N. Luciani, T. Pellegrino, D. Alloyeau, F. Gazeau, *ACS Nano* **2015**, *9*, 7925.

[11] E. Törnqvist, A. Annas, B. Granath, E. Jalkesten, I. Cotgreave, M. Öberg, *PLoS One* **2014**, *9*, e101638.

[12] a) C. Kästner, D. Lichtenstein, A. Lampen, A. F. Thünemann, *Colloids Surf., A* **2017**, *526*, 76; b) J. Volatron, J. Kolosnjaj-Tabi, Y. Javed, Q. L. Vuong, Y. Gossuin, S. Neveu, N. Luciani, M. Hémadi, F. Carn, D. Alloyeau, F. Gazeau, *Sci. Rep*. **2017**, *7*, 10.

[13] M. W. Hentze, M. U. Muckenthaler, B. Galy, C. Camaschella, *Cell* **2010**, *142*, 24.

[14] R. Klingholz, B. Steinkopf, *Biol. Eff. Man-Made Miner. Fibers* **1984**, *2*, 60.

[15] J. G. Keller, W. Peijnenburg, K. Werle, R. Landsiedel, W. Wohlleben, *Nanomaterials* **2020**, *10*, 311.

[16] J. Keller, W. Wohlleben, *nanoGRAVUR* **2018**, *28*, 09.

[17] a) J. G. Keller, U. M. Graham, J. Koltermann-Jülly, R. Gelein, L. Ma-Hock, R. Landsiedel, M. Wiemann, G. Oberdörster, A. Elder, W. Wohlleben, *Sci. Rep*. **2020**, *10*, 458; b) J. Koltermann-Jülly, J. G. Keller, A. Vennemann, K. Werle, P. Müller, L. Ma-Hock, R. Landsiedel, M. Wiemann, W. Wohlleben, *NanoImpact* **2018**, *12*, 29.

[18] C. A. Lanzl, J. Baltrusaitis, D. M. Cwiertny, *Langmuir* **2012**, *28*, 15797.

[19] a) J. Koltermann-Jülly, J. G. Keller, A. Vennemann, K. Werle, P. Müller, L. Ma-Hock, R. Landsiedel, M. Wiemann, W. Wohlleben, *Sci. Rep*. **2020**, *10*, 458; b) Y. Portilla, Y. Fernández-Afonso, S. Pérez-Yagüe, V. Mulens-Arias, M. P. Morales, L. Gutiérrez, D. F. Barber, *J. Nanobiotechnol*. **2022**, *20*, 23.

[20] M. P. Monopoli, C. Åberg, A. Salvati, K. A. Dawson, *Nat. Nanotechnol*. **2012**, *7*, 779.

[21] J. G. Croissant, Y. Fatieiev, N. M. Khashab, *Adv. Mater.* **2017**, *29*, 160463.

[22] T. Kurz, J. W. Eaton, U. T. Brunk, *Int. J. Biochem. Cell Biol*. **2011**, *43*, 1686.

[23] a) W. W. Wang, C. L. Hao, M. Z. Sun, L. G. Xu, C. L. Xu, H. Kuang, *Adv. Funct. Mater.* **2018**, *28*, 8; b) A. A. Demessie, Y. Park, P. Singh, A. S. Moses, T. Korzun, F. Y. Sabei, H. A. Albarqi, L. Campos, C. R. Wyatt, K. Farsad, P. Dhagat, C. Sun, O. R. Taratula, O. Taratula, *Small Methods* **2022**, *6*, 2200916; c) M. A. Kang, J. Fang, A. Paragodaarachchi, K. Kodama, D. Yakobashvili, Y. Ichiyanagi, H. Matsui, *Nano Lett.* **2022**, *22*, 8852.

[24] M. Rabel, P. Warncke, C. Grüttner, C. Bergemann, H.-D. Kurland, R. Müller, V. Dugandzic, J. Thamm, F. A. Müller, J. Popp, D. Cialla-May, D. Fischer, *Nanomedicine* **2019**, *14*, 1681.

[25] C. Kinnear, T. L. Moore, L. Rodriguez-Lorenzo, B. Rothen-Rutishauser, A. Petri-Fink, *Chem. Rev.* **2017**, *117*, 11476.

[26] J. Zeng, L. Jing, Y. Hou, M. Jiao, R. Qiao, Q. Jia, C. Liu, F. Fang, H. Lei, M. Gao, *Adv. Mater.* **2014**, *26*, 2694.

[27] M. Rozalen, M. E. Ramos, F. J. Huertas, S. Fiore, F. Gervilla, *J. Asian Earth Sci.* **2013**, *77*, 318.

[28] H. Zhang, F. Huang, B. Gilbert, J. F. Banfield, *J. Phys. Chem. B* **2003**, *107*, 13051.

[29] a) H. Z. Zhang, B. Chen, *J. Phys. Chem*. **2010**, *114*, 14876; b) D. Panias, M. Taxiarchou, I. Paspaliaris, A. Kontopoulos, *Hydrometallurgy* **1996**, *42*, 257; c) M. A. Blesa, H. A. Marinovich, E. C. Baumgartner, A. J. G. Maroto, *J. Am. Chem. Soc.* **1987**, *26*, 3713.

[30] X. Li, J. J. Lenhart, H. W. Walker, *Langmuir* **2012**, *28*, 1095.

[31] M. Baalousha, *Sci. Total Environ.* **2009**, *407*, 2093.

[32] M. Rabel, P. Warncke, M. Thürmer, C. Grüttner, C. Bergemann, H.-D. Kurland, F. A. Müller, A. Koeberle, D. Fischer, *Nanoscale* **2021**, *13*, 9415.

[33] G. Stepien, M. Moros, M. Pérez-Hernández, M. Monge, L. Gutiérrez, R. M. Fratila, M. D. Las Heras, S. Menao Guillén, J. J. Puente Lanzarote, C. Solans, J. Pardo, J. M. De La Fuente, *ACS Appl. Mater. Interfaces* **2018**, *10*, 4548.

[34] G. Yang, S. Z. F. Phua, A. K. Bindra, Y. Zhao, *Adv. Mater.* **2019**, *31*, 1805730.

[35] R. I. Maccuspie, A. J. Allen, V. A. Hackley, *Nanotoxicology* **2011**, *5*, 140.

[36] a) A. Lesniak, A. Campbell, M. P. Monopoli, I. Lynch, A. Salvati, K. A. Dawson, *Biomaterials* **2010**, *31*, 9511; b) M. S. P. Boyles, T. Kristl, A. Andosch, M. Zimmermann, N. Tran, E. Casals, M. Himly, V. Puntes, C. G. Huber, U. Lütz-Meindl, A. Duschl, *J. Nanobiotechnol*. **2015**, *13*, 84; c) F. Barbero, L. Russo, M. Vitali, J. Piella, I. Salvo, M. L. Borrajo, M. Busquets-Fité, R. Grandori, N. G. Bastús, E. Casals, V. Puntes, *Semin. Immunol*. **2017**, *34*, 52.

[37] a) W. W. Frenier, F. B. Growcock, *Corrosion* **1984**, *40*, 663; b) K. Norén, J. S. Loring, J. R. Bargar, P. Persson, *J. Phys. Chem. C* **2009**, *113*, 7762.

[38] W. Utembe, K. Potgieter, A. B. Stefaniak, M. Gulumian, *Part. Fibre Toxicol*. **2015**, *12*, 11.

[39] L. Lartigue, D. Alloyeau, J. Kolosnjaj-Tabi, Y. Javed, P. Guardia, A. Riedinger, C. Péchoux, T. Pellegrino, C. Wilhelm, F. Gazeau, *ACS Nano* **2013**, *7*, 3939.

[40] M. Unni, A. M. Uhl, S. Savliwala, B. H. Savitzky, R. Dhavalikar, N. Garraud, D. P. Arnold, L. F. Kourkoutis, J. S. Andrew, C. Rinaldi, *ACS Nano* **2017**, *11*, 2284.

[41] J. Curiale, M. Granada, H. E. Troiani, R. D. Sánchez, A. G. Leyva, P. Levy, K. Samwer, *Appl. Phys. Lett.* **2009**, *95*, 043106.

[42] a) J. Lee, J. Yang, S. G. Kwon, T. Hyeon, *Nat. Rev. Mater.* **2016**, *1*, 16034; b) J. Baumgartner, A. Dey, P. H. H. Bomans, C. Le Coadou, P. Fratzl, N. A. J. M. Sommerdijk, D. Faivre, *Nat. Mater.* **2013**, *12*, 310; c) N. D. Loh, S. Sen, M. Bosman, S. F. Tan, J. Zhong, C. A. Nijhuis, P. Král, P. Matsudaira, U. Mirsaidov, *Nat. Chem*. **2017**, *9*, 77; d) Z. Ou, Z. Wang, B. Luo, E. Luijten, Q. Chen, *Nat. Mater.* **2019**, *19*, 450.

[43] J. Dulinska-Litewka, A. Lazarczyk, P. Halubiec, O. Szafranski, K. Karnas, A. Karewicz, *Materials* **2019**, *12*, 617.

[44] a) S. H. Koenig, K. E. Kellar, *Magn. Reson. Med.* **1995**, *34*, 227; b) R. A. Brooks, F. Moiny, P. Gillis, *Magn. Reson. Med*. **2001**, *45*, 1014; c) R. N. Muller, L. Vander Elst, A. Roch, J. A. Peters, E. Csajbok, P. Gillis, Y. Gossuin, *Advances in Inorganic Chemistry*, Elsevier Academic Press Inc, San Diego, CA, USA **2005**.

[45] M. Cho, J. Villanova, D. M. Ines, J. Chen, S. S. Lee, Z. Xiao, X. Guo, J. A. Dunn, D. D. Stueber, P. Decuzzi, V. L. Colvin, *J. Phys. Chem. C* **2023**, *127*, 1057.
[46] E. Pöselt, H. Kloust, U. Tromsdorf, M. Janschel, C. Hahn, C. Maßlo, H. Weller, *ACS Nano* **2012**, *6*, 1619.
[47] S. Xiong, W. Qi, B. Huang, M. Wang, Y. Li, *Mater. Chem. Phys.* **2010**, *120*, 446.
[48] H. Z. Zhang, B. Chen, *J. Phys. Chem.* **2010**, *114*, 14876.
[49] H. T. Ta, Z. Li, Y. Wu, G. Cowin, S. Zhang, A. Yago, A. K. Whittaker, Z. P. Xu, *Mater. Res. Express* **2017**, *4*, 116105.
[50] E. Valero, S. Fiorini, S. Tambalo, H. Busquier, J. Callejas-Fernández, P. Marzola, N. Gálvez, J. M. Domínguez-Vera, *J. Med. Chem.* **2014**, *57*, 5686.